Salt intrusion dynamics in a well-mixed sub-estuary connected to a partially to well-mixed main estuary

Zhongyuan Lin[c,d], Guang Zhang[a,b], Huazhi Zou[c,d], Wenping Gong[a,b*]

[a]School of Marine Sciences, Sun Yat-sen University, Zhuhai, 519082, China

[b]Guangdong Provincial Key Laboratory of Marine Resources and Coastal Engineering, Zhuhai, 519082, China

[c] Key Laboratory of Pearl River Estuary Regulation and Protection of Ministry of Water Resource, Guangzhou 510611, China

[d] Pearl River Water Resource Research Institute, Guangzhou 510611, China

Corresponding Author: Wenping Gong (gongwp@mail.sysu.edu.cn)

Abstract

Salt intrusion in estuaries has been exacerbated by climate change and human activities. Previous studies have primarily focused on salt intrusion in the mainstem of estuaries, whereas those in sub-estuaries (those branch off their main estuaries) have received less attention. During an extended La Niña event from 2021 to 2022, a sub-estuary (the East River estuary)alongside the Pearl River Estuary, China, experienced severe salt intrusion, posing a threat to the freshwater supply in the surrounding area. Observations revealed that maximum salinities in the main estuary typically preceded spring tides, exhibiting significant asymmetry in salinity rise and fall over a fortnightly timescale. In contrast, in the upstream region of the sub-estuary, the variation of salinity was in phase with that of the tidal range, and the rise and fall of the salinity were more symmetrical.

27   Inspired by these observations, we employed idealized numerical models and

28   analytical solutions to investigate the underlying physics behind these behaviors. It was

29   discovered that under normal dry condition (with a river discharge of 1500 m^3 s^{-1} at the

30   head of the main estuary), the river-tide interaction and change in horizontal dispersion

31   accounted for the in-phase relationship between the salinity and tidal range in the

32   upstream region of the sub-estuary. Under extremely dry conditions (i.e., a river

33   discharge of 500 m^3 s^{-1} at the head of the main estuary), salinity variations were in-

34   phase with those of the tidal range in the middle as well as the upstream region of the

35   sub-estuary. The variation of salinity in the main estuary, along with those of salt

36   dispersion and freshwater influx inside the sub-estuary collectively influenced salinity

37   variation in the well-mixed sub-estuary. These findings have important implications for

38   water resource management and salt intrusion prevention in the catchment area.

39   **Keywords**: Sub-estuaries; River-tide interaction; Partially to well-mixed estuary.

41   **1. Introduction**

43   Salt intrusion in estuaries has emerged as an increasingly significant

44   environmental issue, as it contaminates water quality, restricts freshwater supply, and

45   affects the biota's habitat in estuaries (Payo-Payo et al., 2022). The severity of salt

46   intrusion in estuaries has been further exacerbated by both climate change and

47   anthropogenic activities. Climate change has led to more severe droughts in various

regions worldwide (Spinoni et al., 2014), resulting in reduced freshwater flow from upstream watershed basin into estuaries. In turn, this has intensified salt intrusion in these areas. Additionally, sea level rise has been identified as a contributing factor to this phenomenon (e.g., Hong et al., 2020). Human activities, including dam construction in the watershed, channel dredging, and land reclamation in estuaries, have caused reductions in river inflow, channel deepening, and enhanced convergence of estuarine geometry, all of which favor an increase in salt intrusion (e.g., Ralston and Geyer, 2019).

Salt intrusion in estuaries is the result of landward salt transport, which consists of steady shear and tidal oscillatory transport (MacCready and Geyer, 2010). The combination of estuarine circulation and salinity stratification induces a steady shear when averaged in a tidal cycle. Tidal oscillatory transport is generated by tidal pumping such as the jet-sink flow for an inlet (Stommel and Farmer, 1952), tidal trapping with a side embayment (Okubo, 1973), tidal shear dispersion by the vertical shears of current and mixing (Bowden, 1965), tidal straining (Simpson et al., 1990), and chaotic stirring (Zimmerman, 1986).

In general, for a partially mixed estuary in which the steady shear dominates the landward salt transport, the salt intrusion is strongest during neap tides and weakest during spring tides under the steady-state conditions, meaning that the change in salinity is out-of-phase with that in the tidal range. However, for a well-mixed and/or a salt

wedge estuary, in which the tidal dispersion is the dominant contributor to landward

salt transport, the salt intrusion is strongest during spring tides and weakest during neap

tides, signifying that the salinity variation is in phase with the tidal range (Ralston et

al., 2010). These steady-state situations are altered by the unsteadiness of external

forcing and the adjustment of estuaries to the changing forcings (Chen 2015 and

references therein). In general, when the internal timescale of an estuary, which is

defined as the time needed for a water parcel from the upstream to travel through the

estuary by the river-induced flow, is shorter than the external timescale, which is often

the spring-neap tidal cycle, the salinity variation in an estuary can keep pace with the

change in tidal forcing and reaches steady state. However, when the internal timescale

is longer than the external timescale, the salt intrusion can hardly reach the steady state,

and there exists a phase shift between the salt intrusion and tidal range, such as in the

Modaomen estuary (Gong and Shen, 2011) and Hudson River (Bowen and Geyer,

2003).

Previous studies on salt intrusion have primarily focused on main estuaries, where

freshwater discharge empties into the estuarine waterbody at the estuary head and is

profoundly diluted by the seawater from the ocean. However, there has been relatively

less research on salinity dynamics specifically in tidal creeks or sub-estuaries, i.e. those

that reside aside from their main estuary. It is worth noting that larger estuaries often

possess sub-estuaries or tidal creeks, as highlighted by Uncles and Stephens (2010).

88 Sub-estuaries branch off the stem of their main estuary and exhibit behavior that is

89 partially dependent on processes acting within the main estuary. Haywood et al. (1982)

90 described the importance of conditions at the confluence of the York River sub-estuary

91 and the Chesapeake Bay to salinity stratification within the sub-estuary. Uncles and

92 Stephens (2010) investigated the salinity dynamics in a sub-estuary (Tavy) connected

93 to the main estuary (Tamar, UK). They noted that the tidal range had a limited effect on

94 the salinity in the sub-estuary. Yellen et al. (2017) examined the sediment dynamics in

95 a side embayment of the main estuary of Connecticut, USA, and found that salinity

96 intrusion from the main estuary enhanced sediment trapping inside the sub-estuary.

97   The previous studies on sub-estuary salt dynamics have mainly focused on

98 examining salinity variabilities and water column stratification, as exemplified by the

99 work of Haywood et al. (1982). Some investigations have also explored the influence

100 of river discharge from the heads of the main estuary and sub-estuary, as well as the

101 impact of winds, as discussed by Uncles and Stephens (2010). However, there remains

102 a knowledge gap regarding how the salt dynamics in the main estuary affect those in

103 the sub-estuary, as well as how the interaction between river flow and tides influences

104 salinity variations in the sub-estuary. Regarding the river-tide interaction, here we focus

105 on how tides affect river flow through mechanisms such as nonlinear bottom friction

106 and advective terms in the momentum equation, as outlined by Buschman et al. (2009),

107 whereas the effect of river flow on tidal propagation will not be explored.

108   In 2021, under the influence of a La Nina event, the precipitation in the Pearl River

109   Delta (PRD) area (Fig. 1), China, was extremely low, and the salt intrusion was very

110   severe, which imposed a great threat to the freshwater supply in the region, especially

111   during winter months (December to February). Alongside the Pearl River Estuary

112   (PRE), a sub-estuary of the East River estuary (Fig. 1), also experienced strong salt

113   intrusion and heavily impacted the water supply to the city of Dongguan, home to a

114   population of 10 million people. This shortage of freshwater became a significant

115   concern for the surrounding people, especially during the Spring Festival, the Chinese

116   Lunar New Year.
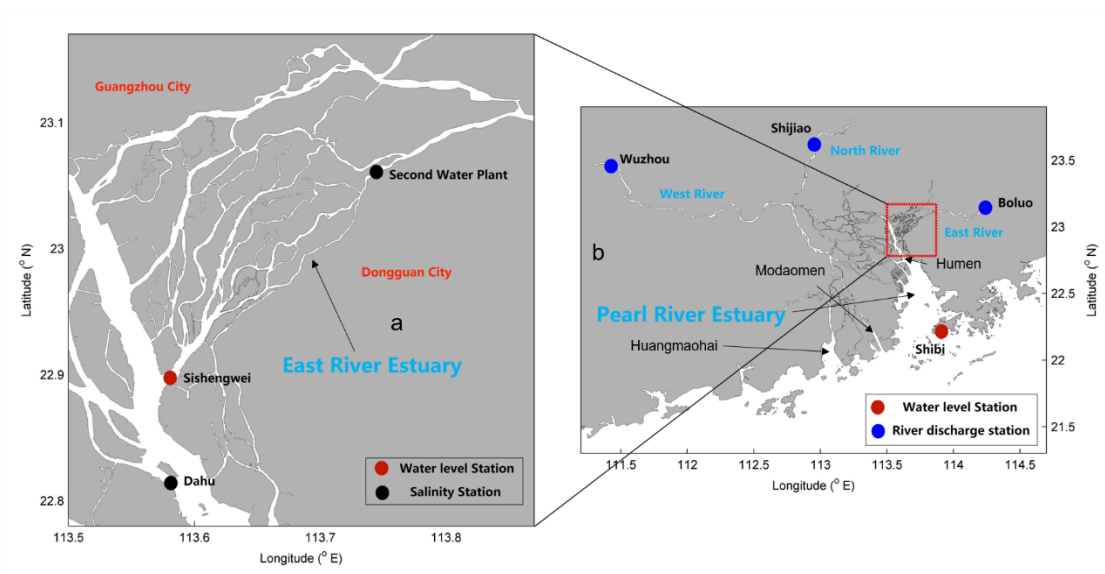
117

118   Fig.1. a) The East River estuary; b) Map of the Pearl River Delta and the locations of hydrological

119   and water level stations.

120

121   The present work has two objectives: (a) to investigate the characteristics of salt

intrusion in a well-mixed sub-estuary by analyzing observation data. The characteristics

include spatial-temporal variations of salt intrusion and its relationship with river flow

and tidal range; (b) to explore the underlying physics behind salt intrusion in the sub-

estuary, such as the impacts of salt dynamics in the main estuary, and the river-tide

interaction inside the sub-estuary. To achieve the above goals, we first collected and

analyzed observational data of salt intrusion at the East River estuary. Then we utilized

an idealized configuration for numerical model investigation. Two numerical model

experiments with mean and extremely low river discharges in dry seasons in the main

estuary, respectively, were conducted to identify the relevant mechanisms for the

variability of salt intrusion in the sub-estuary. Furthermore, to clearly understand the

phase relationship between salinity and tidal range, analytical solutions for the tidally-

averaged salinity in the well-mixed sub-estuary were utilized. In this study we set a

tidal period to be 25 hours. The remainder of this paper is structured as follows. The

study site is briefly introduced in Section 2. The methods of data analysis, numerical

model simulation, and analytical solution are presented in Section 3. In Section 4, the

results of the salt intrusion dynamics through the measurement data analysis, numerical

model, and analytical solution are demonstrated, followed by some discussions on the

impacts of river-tide interaction in the sub-estuary, the salt dynamics in the main estuary,

and the limitations of this study in Section 5. Finally, a summary and conclusion are

given in Section 6.

2. Study site

The Pearl River, China's second largest river in terms of annual freshwater discharge, has three main branches: West River, North River, and East River (Hu et al., 2011), as displayed in Fig. 1b. The Pearl River forms a complex delta, known as the Pearl River Delta (PRD), which consists of the downstream river network and three estuaries, from west to east: the Huangmaohai Estuary, the Modaomen Estuary, and the PRE (Fig. 1b). The PRE, the largest of the three estuaries, is funnel-shaped and has a mean depth of 4.6 m (Wu et al., 2016). Its width decreases from 50 km at its mouth between Hong Kong and Macau to 6 km at Humen Outlet. The axial length of the estuary from the mouth to Humen is approximately 70 km. Above the Humen, the estuary becomes relatively straight and further extends almost 90 km landward to its head. Upstream of the Humen, there exists a waterway known as Shizhiyang. Along the waterway, there are several river tributaries, among which the East River sub-estuary, are distributed on the east side.

The river discharge dumping into the PRE is about 1/4 of the total river flow from the Pearl River. The total annual river flow of the Pearl River is 3260×10^8 m^3, in which the river flow experiences distinct seasonal variations. During the dry season (from November to March), the river flow takes up only about 30% of the total annual flow, that is about 6000 m^3/s, and the river discharge into the PRE is 1500 m^3/s (1/4 of the

163   total). Under extremely dry conditions, the river discharge into the PRE can be less than

164   1000 m^3/s.

165   The PRE has a microtidal and mixed semi-diurnal regime (Mao et al., 2004). The

166   annual mean tidal range is 1.45 m near Lantau Island (at the mouth of the PRE) and

167   1.77 m near the Humen outlet (Gong et al., 2018). The amplitudes of M_2, S_2, K_1, and O_1

168   constituents near the Lautau Island are 35.5, 14, 33.5, and 27.9 cm, respectively (Mao

169   et al., 2004), showing the dominance of the M_2 constituent. The alternation of neap and

170   spring tides causes the tidal range near Lantau Island to vary from approximately 0.7 m

171   during neap tides to approximately 2 m during spring tides. Apart from the fortnightly

172   variation of the tidal range, there also exists a monthly variation, which is referred to as

173   the apogee/perigee cycle (Payo-Payo et al., 2022).

174   The PRE exhibits strong seasonal variation and is highly stratified during the wet

175   summer season (July to September), with the bottom isohaline of 10 g/kg protruding

176   into the upper estuary (50 to 70 km from the estuary mouth) and the surface isohaline

177   of 10 g/kg extending outside of the estuary. The tidally-averaged bottom-surface

178   salinity difference is mostly greater than 10 g/kg inside the estuary (Dong et al., 2004).

179   During the dry season, the PRE is generally in a partially mixed state, with the bottom

180   isohaline of 10 g/kg reaching the Humen Outlet, and the surface isohaline of 10 g/kg

181   lying in the upper estuary (Wong et al., 2003; Gong et al., 2018). In the dry season, the

182   horizontal difference of depth-mean salinity varies by between 20 and 25 g/kg across a

distance of 70 km from the estuary mouth to Humen Outlet, and the vertical salinity difference between the surface and bottom varies from 1 to 12 g/kg along the channels in the estuary.

The East River is a branch of the Pearl River, with a length of 562 km and a drainage area of 27,040 km^2. It forms a sub-delta, known as the East River Delta, which is located on the east side of the PRE and above the Humen Outlet (Fig. 1a). The upper reach of the East River is essentially composed of a single channel, while in its lower reach, downstream of Dongguan City, a complex river network is formed, including several tributaries (Fig. 1a). Here we focus on the southernmost tributary, which merges into the main estuary at the confluence of Sishengwei, where a hydrological station resides. This tributary has a length of approximately 75 km from the confluence (Sishengwei) to the upstream hydrological station of Boluo (Fig. 1b), and a mean water depth of less than 5 m.

The average annual freshwater load of the East River is 240×10^8 m^3, or a mean river discharge of 728 m^3 s^{-1}, accounting for 7.1% of the total river flow of the Pearl River. During dry seasons, the river discharge is approximately 400 m^3 s^{-1}. However, the annual mean river discharge in 2021 was only 262 m^3 s^{-1}. During the winter of 2021, the salinity at several water plants exceeded the drinking water criteria of 0.5 g/kg for a lasting duration of 3 months and impaired the freshwater supply in the region.

Similar to the main estuary, the tidal regime in the East River sub-estuary is a

203   mixed semi-diurnal one, with the tidal range decreasing when propagating upstream

204   due to the predominance of the bottom friction over the estuarine convergence. In recent

205   decades, the tidal strength has been seen to increase by human activities, such as sand

206   mining in the estuary (Jia et al., 2006).

207

208   **3. Methods**

209

210   **3.1 Observation data and analysis**

211

212   The observation data here consist of the daily discharge of the West, North, and

213   East Rivers, hourly water level data at the confluence (Sishengwei) between the East

214   River sub-estuary and the main estuary (PRE), daily sea level at the mouth of the PRE

215   (Shibi), and hourly surface salinity data at the Dahu station, which is located

216   downstream of the Sishengwei, and at the Second Water Plant of Dongguan City. These

217   two stations span a distance of approximately 30 km. The river discharge data at three

218   river branches of the Pearl River, hourly water level data at Sishengwei, and hourly

219   surface salinity data at Dahu are from the Pearl River Water Resources Commission,

220   whereas the salinity data at the Second Water Plant is from the Water Authority of

221   Dongguan City. The sea level data at the estuary mouth is from the Hong Kong

222   Observatory (http://gb.weather.gov.hk/contentc.htm). All the salinity data are the

223   surface salinities.

224   The salinity data at the Second Water Plant was subject to wavelet analysis, a

225   method that has been widely used to analyze geophysical data, like in salt intrusion

226   studies in estuaries (Liu et al., 2014; Gong et al., 2022). This method can identify

227   localized periodicities (or bands) that are linked to specific processes, such as tidal and

228   spring-neap variations. In this study, the continuous wavelet transform (CWT) method

229   was used to identify the multi-scale characteristics of salinity, and cross wavelet was

230   employed to examine the nonlinear correlations among variables, such as between the

231   salinity of the Second Water Plant and the water level at Sishengwei, between the

232   salinity of the Second Water Plant and the salinity of Dahu, and between the salinity of

233   the Second Water Plant and the river discharge at the Boluo Station.

234

235   **3.2 Numerical model configuration and experiments**

236

237   The Regional Ocean Modeling System (ROMS) was used in this modeling study.

238   ROMS is a free-surface, hydrostatic, primitive-equations ocean model that uses

239   stretched, terrain-following vertical coordinates and orthogonal curvilinear horizontal

240   coordinates on an Arakawa C-grid (Haidvogel et al. 2000). The model domain was

241   designed as an estuary-shelf system (Fig. 2). In the coordinate system, x is in the
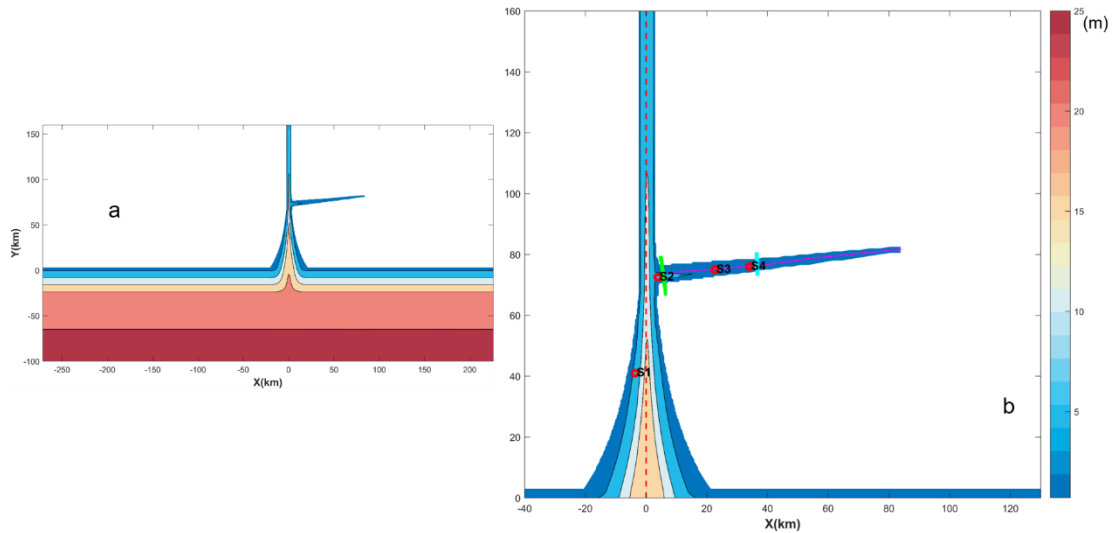
242

Fig. 2. Geometry and bathymetry of the idealized model domain: a) for the whole domain; b)

zoom in for the area of concern. The origin of the coordinates is in the middle of the main estuary

mouth. The longitudinal sections in the main and sub-estuary are shown as dashed lines, and the

cross-sections inside the sub-estuary are shown as color solid lines. The locations of several

stations are indicated.

cross-estuary direction, with rightward being positive, y is in the along-channel

direction, with landward being positive, and z directs upward. The origin of the

system is in the middle of the estuary mouth. The estuary is composed of a convergent

part and a straight part. The geometry and bathymetry of the estuary roughly resemble

those of the PRE, with the convergent part extending from the estuary mouth to the

Humen Outlet (70 km in length), and the straight part from the Humen Outlet to the

head of the estuary (90 km long). For the convergent part, the estuarine width B is

assumed to decrease exponentially in the landward direction, as follows:

$$B = B_0 \exp(-\frac{y}{L_b}) \qquad (1)$$

257

258   where B_0 is the estuarine width at the estuary mouth (here taken as 46 km) and L_b is

259   the width convergence length (taken as 31 km, as estimated by Zhang et al., 2021). The

260   bathymetry of the PRE is characterized by deep channels and side shallow shoals.

261   Following Wei et al. (2017), we roughly mimicked this feature by setting the

262   bathymetry of the convergent part as:

263    $$H(x,y) = H_{min} + (H_m - H_{min})\frac{y}{L} + (H_{max} - H_{min}) \times \left(1 - \frac{y}{L}\right)\left(1 - \frac{4x^2}{B^2}\right)e^{-C_f\left(\frac{4x^2}{B^2}\right)} \qquad (2)$$

264   where L is the length of the convergent part (70 km); H_{max} (20 m) and H_{min} (3.0 m)

265   are the maximum and minimum water depths at the estuary mouth, the width-averaged

266   water depth H_m is constant (H_m= 8 m) along the estuary, and the parameter C_f is set

267   as 4, based on the bathymetry data. In the straight part of the estuary, the bathymetry

268   was kept the same as that of the uppermost cross-section of the convergent part.

269   At a distance of 75 km from the mouth of the main estuary, we added a sub-estuary

270   on the east side, resembling the East River sub-estuary. The sub-estuary extends in a

271   southwest-northeast direction for a distance of approximately 75 km. The width of the

272   sub-estuary is convergent, with a width of 10 km at the confluence and decreasing to

273   600 m at the head, with an e-folding decrease scale (L_b) of 26.7 km. The water depth

274   decreases landward from 6 m at the confluence to 3.5 m at the head of the sub-estuary.

275   As the boundary conditions at an estuary mouth are generally unknown, we added

276   a continental shelf to the model domain. The shelf is 100 km wide and approximately

277   500 km long, with the downstream part (representing the Kelvin wave propagation

278   direction) being slightly longer than the upstream part. The water depth of the shelf is

279   uniform in the alongshore direction and increases linearly from the coast to the offshore

280   direction, with a slope of 1×10^{-4}. The model grid has 313×506 cells, with a cross-

281   channel spatial resolution of 300 m and an along-channel resolution of 500 m in the

282   estuary. The horizontal resolution decreases on the shelf and becomes 2 km at the open

283   ocean boundaries. Fifteen vertical s-grid layers were specified with higher resolutions

284   near the surface and bottom, and the coefficients of θ_s, θ_b, and h_c were set as 2.5,

285   3.0, and 5.0, respectively. In ROMS Model, coefficients larger than unity for θ_s, θ_b

286   can generate higher resolutions near the surface and bottom, respectively. For details of

287   these coefficients, Shchepetkin and McWilliams (2005) can be referred to.

288   We used the $k-\varepsilon$ submodel of the Generic Length Scale (*GLS*) turbulence

289   closure scheme to calculate the vertical mixing (Umlauf and Burchard, 2003; Warner

290   et al., 2005). The horizontal eddy viscosity and diffusivity were calculated using the

291   Smagorinsky scheme (Smagorinsky, 1963). The bottom friction was calculated based

292   on the log-layer assumption near the bottom, with a bottom roughness length of 1 mm.

293   This setting results in a mean bottom drag coefficient of 0.005. The open ocean

294   boundary condition for the barotropic component consists of a Flather/Chapman

295   boundary condition for the depth-averaged flow and sea surface elevation (Chapman,

296   1985; Flather, 1976). The open boundary conditions for the temperature, salinity, and

297   baroclinic current are the Orlanski-type radiation conditions (Orlanski, 1976).

298   To investigate the impact of salt dynamics in the main estuary on salt intrusion in

299   the sub-estuary, two numerical experiments were implemented. In both cases, the river

300   discharge at the head of the sub-estuary was set as 200 m³/s, which is approximately

301   the value during the dry season in 2021 in the East River estuary. A time series of water

302   levels produced by a combination of 12 tidal constituents was specified at the offshore

303   boundary. These 12 tidal constituents are M_2, S_2, N_2, K_2, K_1,

304   O_1, P_1, Q_1, M_4, MS_4, M_m, M_f, respectively. The tidal constants of these 12

305   constituents were obtained from the Oregon Tidal Database (OPTS). As the tidal

306   amplitudes are almost doubled at the mouth of the main estuary due to the

307   superimposition of propagating and reflected tidal waves, the amplitudes of these tidal

308   constituents at the offshore boundary were reduced by half. Case 1 was set with a river

309   discharge of 1,500 m³ s⁻¹ at the main estuary's head. The river discharge of 1500 m³ /s

310   is representative of the total amount that empties into the PRE from different outlets in

311   dry seasons (Gong et al., 2020), being lumped as input at the head of the PRE. The

312   inflowing river water was prescribed to have zero salinity and a temperature of 22℃,

313   identical to the background temperature setting throughout the entire domain. The

314   incoming salinity at the offshore boundary was specified to be 34 g/kg. In Case 2, we

315   set an extremely low river discharge (500 m³ s⁻¹) at the head of the main estuary, which

316   is realistic under the La Nina event. In this scenario, we aimed to check how the salt

317 dynamics in the more mixed main estuary affect the salinity variation in the sub-estuary.

318

319 **3.3 Analytical solutions for the salinity variation in the well-mixed sub-estuary**

320

321   For the tidally-averaged salinity variation along the well-mixed sub-estuary, the

322 advection-diffusion equation can be written as:

323 $$\frac{\partial (A\overline{S})}{\partial t} = -\frac{\partial}{\partial x}\left(A\overline{u}\overline{S}\right) + \frac{\partial}{\partial x}\left(AK_x \frac{\partial \overline{S}}{\partial x}\right)$$ (3)

324 where A is the cross-sectional area, $\overline{S}$ is the tidally-averaged salinity in the cross-

325 section, t is time, $\overline{u}$ is tidally-averaged longitudinal velocity, x is the distance along

326 the sub-estuary, K_x is the longitudinal dispersion coefficient. The left term in Eq. 3

327 indicates the local acceleration and the unsteadiness of salinity variation. The

328 unsteadiness is controlled by the contrast between the internal and external timescales.

329 Savenije (2012) suggested an internal timescale to quantify the sub-estuary's response

330 timescale (T_S), which is expressed as:

331 $$T_S = -\frac{1}{Q_f \overline{S}(X)} \int_X^L A\overline{S} dx$$ (4)

332   Based on the numerical model results, by selecting X at the sub-estuary's mouth,

333 we calculated the response timescale to be 16.22 day, which is comparable to the spring-

334 neap tidal cycle. This indicates that the salinity in the sub-estuary can vary along with

335 the changing tidal forcing. We thus ignored the unsteadiness term and assumed that the

336 horizontal dispersion is constant in a tidal period and scales with the tidal current at the

337 sub-estuary's mouth. Meanwhile, the boundary condition of tidally-averaged salinity at

338   the sub-estuary's mouth was updated at each tidal period. In this way, the calculation

339   of tidally-averaged salinity in the sub-estuary can proceed. As such, Eq. 3 becomes (Cai

340   et al., 2015):

$$\frac{Q}{A}\overline{S} = K_x \frac{\partial \overline{S}}{\partial x} \tag{5}$$

341

342   in which Q is the river discharge. We assume that the cross-sectional area decreases

343   exponentially in the landward, $A = A_0 \exp(-x/a)$, where a is the convergence

344   length scale of the cross-sectional area. When the longitudinal dispersion coefficient

345   K_x is assumed to be a constant along the sub-estuary, the tidally-averaged salinity along

346   the sub-estuary can be obtained as:

$$\frac{\overline{S}}{S_0} = \exp\{-\frac{Qa}{A_0 K_x}\left[\exp\left(\frac{x}{a}\right) - 1\right]\} \tag{6}$$

347

348   For each tidal period, we obtained the tidally-averaged salinity (S_0) and the tidal

349   current at the mouth of the sub-estuary from the numerical model results, and related

350   the horizontal dispersion (K_x) to the tidal strength at the mouth. When these data were

351   available, the tidally-averaged salinity at each tidal period was calculated for our

352   numerical simulation period.

353   When the K_x is assumed to vary along the estuary, the salinity variation along the

354   sub-estuary is in another form and not presented here (Savenije, 2012), as that form of

355   K_x is not related to the tidal strength and is unsuitable for our situation here, so this

356   scenario is not pursued further.

357

358   **3.4 Calculation of the salt and freshwater fluxes**

359

360   The salt flux at a cross-section is calculated as follows:

$$F_s = \int uSdA \tag{7}$$

where u is the instantaneous longitudinal velocity, and S is the instantaneous salinity. The instantaneous flux was integrated and then averaged over a tidal period.

As the changes in freshwater transport by the river-tide interaction are concerned, we also calculated the freshwater flux, which is:

$$F_f = \int u(1 - \frac{S}{S_0})dA \tag{8}$$

where S_0 is the ocean salinity, here is taken to be 34 g/kg. The freshwater flux was also integrated and averaged over a tidal period.

4. Results

4.1 The characteristics of salt dynamics in the sub-estuary: based on observation data

Here we take the Second Water Plant as a representative station in the upstream region of the sub-estuary. The salinity variation at this station was checked from 2009 to 2022, as shown in Fig. 3. It indicates (Fig. 3a) that before 2021, the surface salinity was generally lower than 0.5 g/kg and suitable for extraction. During the winter season of 2021-2022, the salinity exceeded the drinking water criterion for a prolonged period of 280 hours in January 2022 (Fig. 3b). These elevated salinities coincided with the decreased river discharge from the upstream in the PRD, shown by the data at the hydrological stations of Boluo, Wuzhou and Shijiao (Figs. 3c, 3d and 3e). Note that the river discharges in 2022 are comparable to those of 2009, but the effect on salinities are

384   dramatically higher. The reasons behind such a difference is not clear right now, but

385   could be due to the increased water depth along the sub-estuary in 2022 by sand mining,

386   and/or the elevated water level outside the sub-estuary due to wind effects.
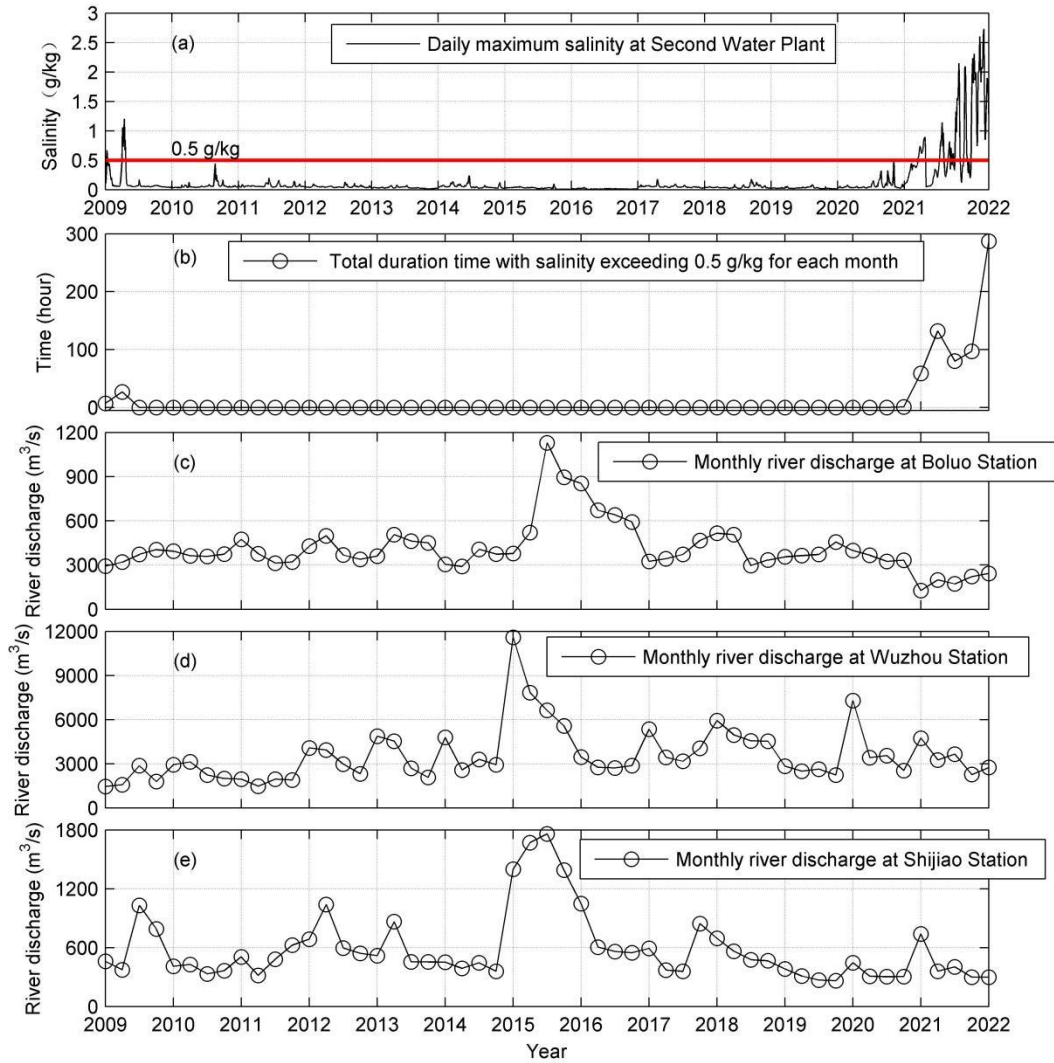
387

388   Fig.3. Timeseries of: a) Daily maximum salinity at the Second Water Plant; b) Total duration

389 period with salinity exceeding 0.5 g/kg for each month; c) Monthly river discharge at Boluo station

390 (upstream of the East River); d) Monthly river discharge at Wuzhou station (upstream of the West

391 River); e) Monthly river discharge at Shijiao station (upstream of the North River).

392

We conducted wavelet analysis for the salinity data of the Second Water Plant Station from September 2021 to February 2022, when the salt intrusion was severe. The result is shown in Fig. 4. It indicates that the power of salinity variations is concentrated in several periods: one is in the range of 0.5 to 1 day, which is caused by tidal fluctuation; the second period lies in the range of 5-9 days, which is presumably induced by wind forcing; the third one is in the range of 14-16 days, obviously by the fortnightly variation of spring-neap tidal cycle. The last one is within the range of 28 days, near the monthly timescale. This periodicity should be caused by the tidal beating among tidal constituents of M_2, S_2, N2, K_1, O_1, as indicated by Payo-Payo et al. (2022).

402
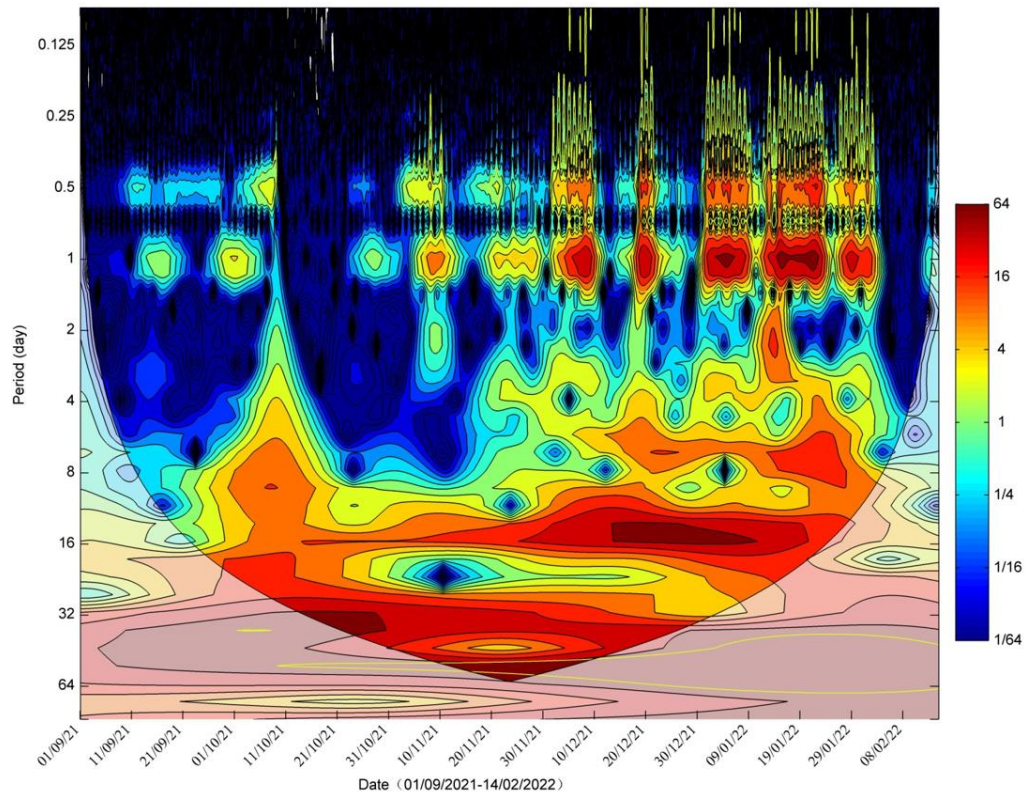
Fig. 4 Wavelet analysis of the salinity at the Second Water Plant

404

To identify the possible factors influencing the salinity variations in the sub-estuary, we present the time series data of salinity at the Second Water Plant, river discharge at Boluo station, tidal range at Sishengwei station, salinity at Dahu station (located in the main estuary), and daily sea level at Shibi station (located at the mouth of the main estuary) in Fig. 5. Firstly, it is evident that the variation of salinity at Dahu (Fig. 5d) shows a consistent pattern with the changes in tidal range at Sishengwei (Fig. 5c), when the river discharge is relatively low after a flash flood event, which occurred around October 21, 2021 (Fig. 5b). The highest salinity happened 2-3 days after neap

413   tides in the transition from neap to spring tides, whereas the lowest salinity occurred in

414   the transition from spring to neap tides, and generally occurred just before the neap

415   tides. This result indicates that the salinity and tidal range in the main estuary were

416   almost out of phase, and there existed a time lead of the salinity to the tidal range. This

417   pattern agrees well with what occurred in the Hudson River (Bowen and Geyer, 2003)

418   and the Modaomen Estuary (Gong and Shen, 2011), suggesting that the PRE remained

419   in a state of partially mixed. On the other hand, the salinity of the Second Water Plant

420   was almost in phase with the tidal range at the confluence (Fig. 5a vs. 5c). High

421   salinities coincided with spring tides, and low salinities occurred during neap tides. It

422   should be noted that the sea level at the PRE mouth showed a significant setup near

423   October 11, 2021, when a large increase in river discharge was observed in the PRD

424   due to a tropical storm (enumerated as the 17th typhoon in 2021, see the peak in Fig.

425   5b). This event caused a sharp decline in salinities at both Dahu and the Second Water

426   Plant, followed by a rebound approximately 10 days later. Note that it takes about 7-8

427   days after the storm for the salinity to recover to its pre-storm levels in the main estuary

428   and almost a month in the sub-estuary. The recovery time is mostly determined by the

429   landward salt flux, as pointed out by Du and Park (2019). The landward salt flux is larger

430   in the main estuary as it is more stratified and the estuarine circulation is more developed,

431   which generate a larger steady shear transport. Meanwhile the width and the cross-sectional

432   area of the main estuary are larger, favorable for the salt import from the ocean. Moreover,

433   the station at the main estuary is located downstream of the confluence between the main

434   estuary and the sub-estuary. After the salinity recovery at the station in the main estuary,

435   the elevated salinity then propagates from the confluence to the upstream of the sub-estuary,

436   where the station at the sub-estuary is located. As the cross-section at the confluence is

437   small, the landward salt flux is limited, further increasing the recovery time for the station

438   at the sub-estuary.
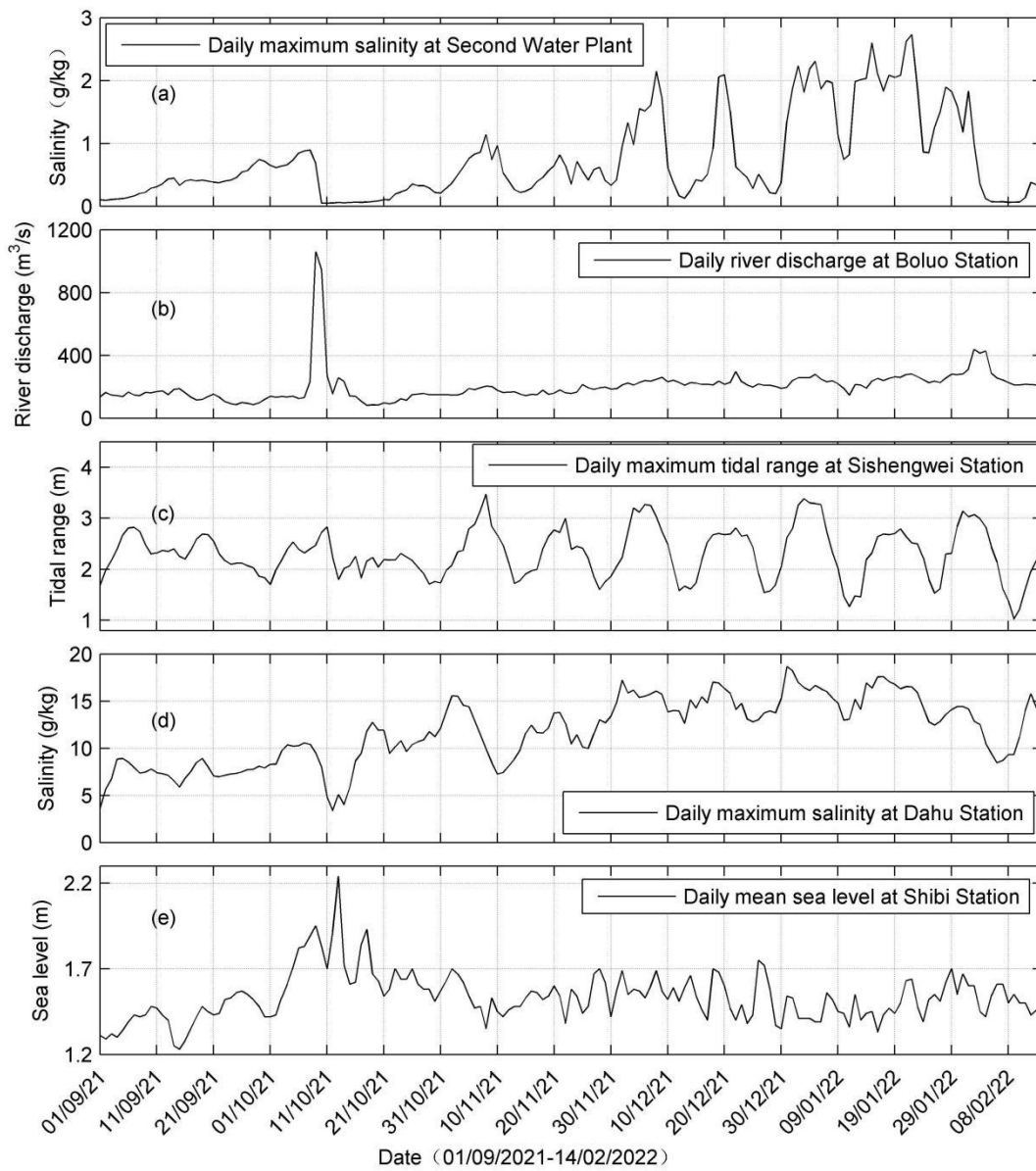
439

440   Fig. 5. Timeseries of: a) Daily maximum salinity at the Second Water Plant; b) Daily river

441   discharge at Boluo station; c) Daily maximum tidal range at Sishengwei Station; d) Daily

442   maximum salinity at Dahu Station; e) Daily mean sea level at Shibi Station.

443

444   The cross-wavelet analysis between salinity at Dahu and tidal range at Sishengwei

445 (Figs. 6a) shows that the two variables are highly correlated in the periods of 14-16

446 days, indicating the effect of fortnightly spring-neap tidal variation. The arrow pointing

447 down and right in this time band demonstrates that the change in tidal range lagged the

448 variation of salinity.
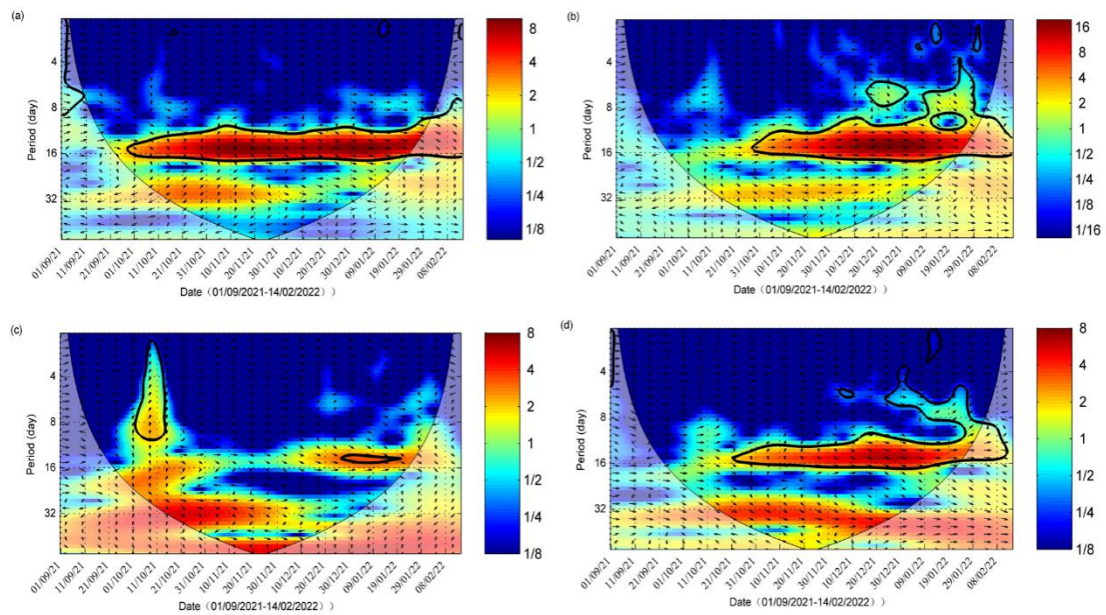
450   Fig. 6. Cross-wavelet analysis of (a) between the salinity at Dahu and the tidal range at

451 Sishengwei; (b) between the salinity at the Second Water Plant and the tidal range at Sishengwei;

452 (c) between the salinity at the Second Water plant and the river discharge at the Boluo Station; (d)

453   between the salinity at the Second Water plant and that at the Dahu Station.

454

455   The cross-wavelet analysis between the salinity at the Second Water Plant and the

456   tidal range at Sishengwei station (Figs. 6b) shows that there existed a high common

457   power band of 14-16 days after October 21, 2021, and the phase relationship between

458   them was in phase, indicating that high salinities occurred during spring tides and low

459   salinities during neap tides, confirming the above results. It is also noted that before the

460   flood event on October 11, 2021, there was no high common power between these two

461   variables, even though the river discharge at the head of East River (Boluo Station) was

462   lower. This lack of high common power in the time band of 14-16 days before the

463   tropical storm event can also be noted in the cross-wavelet analysis between the salinity

464   at Dahu and the tidal range at Sishengwei. We also noted that before the storm event,

465   the water level at Sishengwei did not show distinct fortnightly spring-neap variations

466   (Fig. 5c). This lack of fortnightly cycle could be induced by the wind-induced

467   setup/setdown and/or the river-tide interaction, in which the river flow suppress the

468   tidal propagation. This phenomenon is peculiar and warrants a future study but beyond

469   the scope of this study.

470   The cross-wavelet analysis between the salinity at the Second Water Plant and the

471   river discharge at Boluo Station is presented in Fig. 6c. The high correlation during the

472   storm event was obvious, whereas, after that, the common power between the salinity

473 and river discharge was relatively low during the rebound period of the salinity at the

474 Second Water Plant. This low correlation could be due to the fact that the river discharge

475 did not change much and had no periodicity of 14-16 days then.

476   To examine the relationship between the salinities in the main estuary and at the

477 sub-estuary, we conducted a cross-wavelet analysis between the salinity at the Second

478 Water Plant and that at Dahu (Fig. 6d). There existed high common power between

479 these two variables in the time band of 14-16 days, the fortnightly tidal cycle. It also

480 shows that before October 21, 2021, the phase relationship between these two variables

481 was approximately in quadrature, indicating that the variation of the salinity at the

482 Second Water Plant lagged that at Dahu by 3.5-4 days. After October 21, 2021, the

483 phase relationship between them changed to in-phase when the river discharges in the

484 PRD became very low. This is quite interesting and will be explored in the following.

485

486 **4.2 The salt dynamics obtained through numerical simulations**

487

488   For Case 1 (base run), we intended to investigate the salt dynamics when the main

489 estuary stays in a state of partially mixed. Firstly we examine the variation of salt

490 intrusion length along the estuary's deep channel (Fig. 2b). Here the salt intrusion

491 length is defined as the distance of the bottom salinity isohaline of 5 g/kg from the

492 estuary mouth. It shows that the tidal range at the main estuary's mouth fluctuates at

493 fortnightly and monthly timescales. There occur two spring tides and neap tides in a

month (Fig. 7a), with one spring (neap) tide being stronger than the other one, as the

perigee/apogee cycle. The salt intrusion in the main estuary fluctuates with the tidal

range (Fig. 7b). The maximum salt intrusions occur just after neap tides, and the

minimum salt intrusions occur 2-3 days before neap tides, consistent with the salinity

change at the Dahu station shown above (Fig. 5d), and the results we have demonstrated

before (Gong et al., 2018). The relationship between the salt intrusion and tidal range

indicates an almost anti-phase one, suggesting that the estuary is basically in a state of

partially-mixed. This is because, for a partially-mixed estuary, the landward salt

transport is maximum during neap tides by the steady shear and results in a maximum

salt intrusion then. We present the tidally averaged longitudinal profile of current and

salinity for representative neap and spring tides in Fig. S1 in the Supplement. The

results confirm that during the neap tide, the estuary is partially mixed, whereas, during

the spring tide, the estuary becomes more mixed but still in the state of partially mixed.
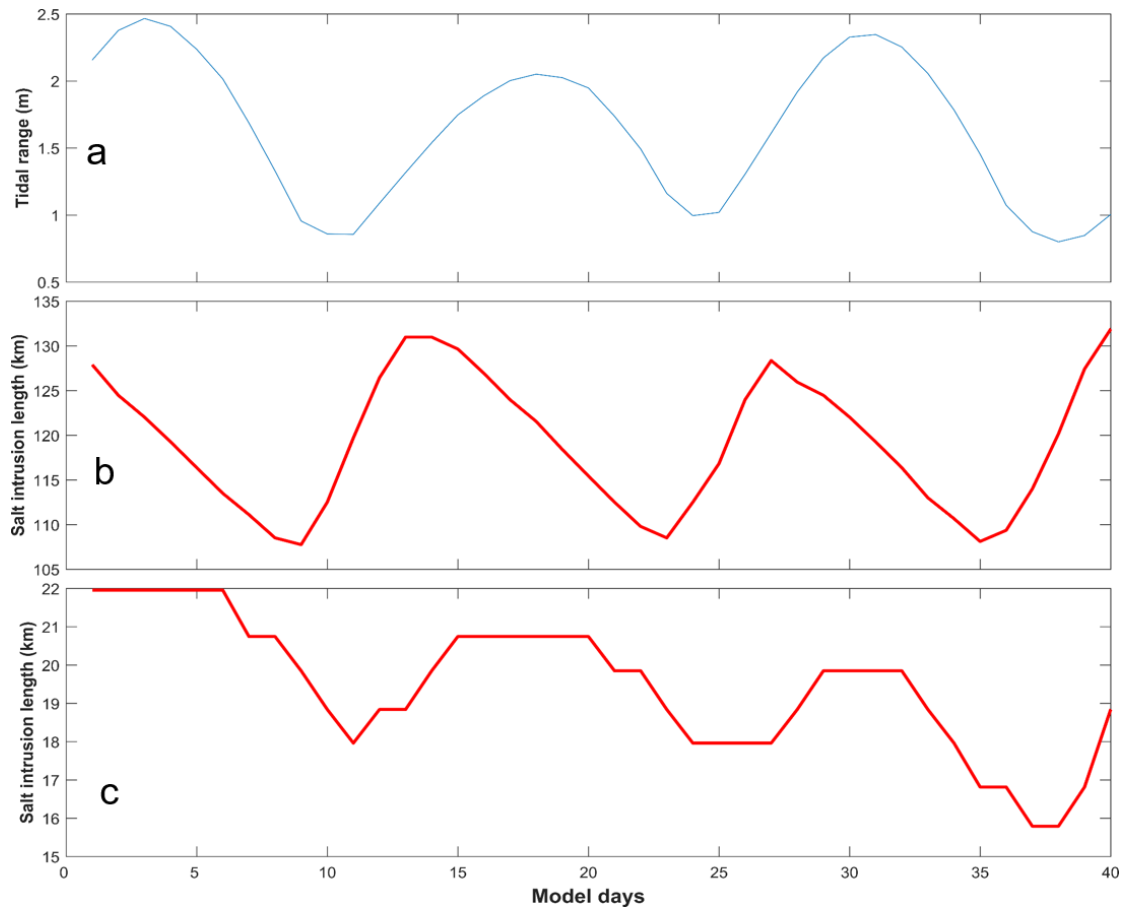
507

Fig. 7. Timeseries of: a) tidal range at the mouth of the main estuary; b) salt intrusion length along

the longitudinal section of the main estuary; c) salt intrusion length along the longitudinal section

of the sub-estuary.

We also checked the time series data of surface salinity and water level at a station

(S1, Fig. 2b) in the main estuary, roughly corresponding to the Dahu Station (Fig. 8a).

It shows that the surface salinity increases from neap to spring tides, and reaches

maxima before spring tides. It declines from the maxima to minima from spring to neap

tides, reaching the minima almost at neap tides. This shows that the salinity increases

517   faster from neap to spring than decreases from spring to neap. This asymmetry is also

518   noted in the variation of salt intrusion length, which increases sharply after the neap

519   tides but decreases more gradually from the maximum to the minimum. This

520   phenomenon has been discussed by Chen (2015); when the salt intrusion length is

521   shorter just before the neap tide, the acceleration by the net landward salt flux is stronger,

522   whereas when the salt intrusion length is longer, the deceleration of salt intrusion length

523   by net seaward salt flux is relatively weaker. The change in salinity leads that in tidal

524   range during spring tides but lags the tidal range during neap tides.
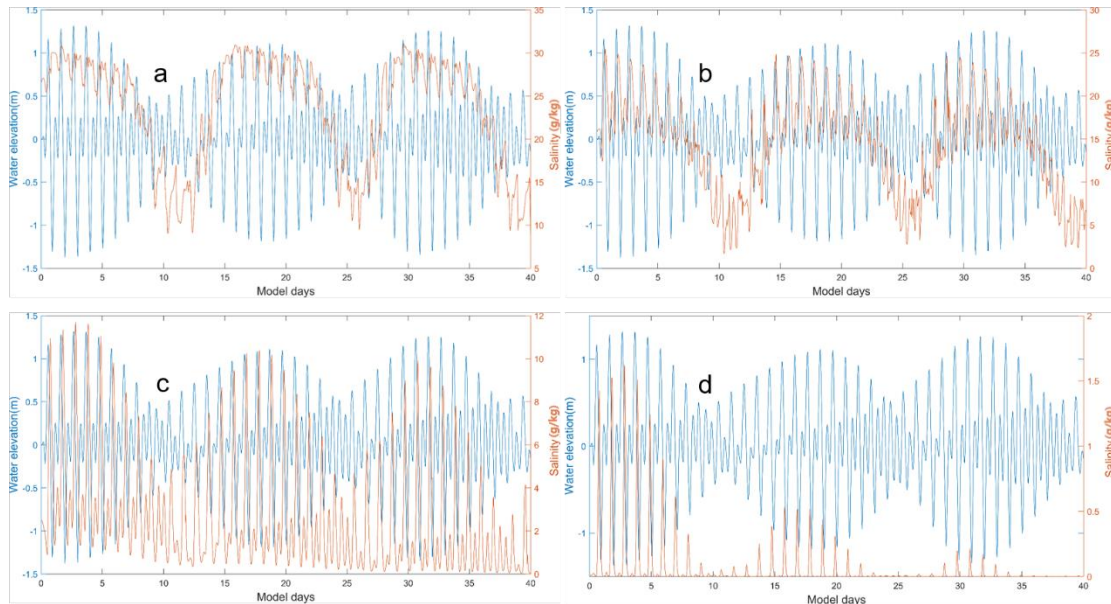
525

526   Fig. 8. Timeseries of water level at the confluence and surface salinity a) at S1 Station in the main

527   estuary; b) at S2 station (the confluence); c) at S3 station in the middle of the sub-estuary; d) at S4

528   station in the upstream region of the sub-estuary.

529

530   Similar to the analysis of observation data, we then investigate the salt intrusion

531   in the sub-estuary (Fig. 7c). Though the accuracy is not high, as our model resolution

532   in the sub-estuary is not fine enough, it clearly shows that the maximum salt intrusions

533   occur nearly in spring tides and the minimum salt intrusions in neap tides. This means

534   that the salt intrusion is in phase with the tidal range in the sub-estuary. We show the

535   tidally averaged profiles of current and salinity at the sub-estuary in Fig. S2 in the

536   Supplement. It indicates that the sub-estuary is mostly in a state of well-mixed during

537   both the neap and spring tides, though there appears some stratification near the mouth

538   of the sub-estuary during the neap tide. The 1 g/kg isohaline intrudes more in spring

539   tides than in neap tides. It should be noted that at the lower reach of the sub-estuary, the

540   surface salinity has a local high salinity zone (Fig. S2), consistent with the finding of

541   Haywood et al. (1982) at the lower York River in the Chesapeake Bay, USA.

542   To examine the salinity variations along the sub-estuary, we selected three stations

543   in the sub-estuary: one at the mouth (S2), one in the middle reach (S3), and the last one

544   in the upper reach (S4). The time series of water level at the confluence and salinities

545   at these three stations are shown in Figs. 8b, 8c and 8d. The salinity at the mouth of the

546   sub-estuary (Fig. 8b) fluctuates similarly to that in the main estuary: maximum salinities

547   occur right after neap tides and minimum salinities just before neap tides. In the middle

548   of the sub-estuary (Fig. 8c), the salinity variation almost keeps pace with that of the

549   tidal range: maximum salinities occur at spring tides and minimum salinities at neap

550   tides. At the upstream station, the salinity variation shows a similar pattern to that in

551 the middle of the sub-estuary. This indicates that when saline water propagates

552 upstream, it advances more landward and experiences less impedance during spring

553 tides and vice versa. We explore this phenomenon in the discussion part.

554

555 **4.3 The tidally-averaged salt dynamics in the sub-estuary by the analytical**

556 **solution**

557

558 We used the analytical solutions in Section 3.3 to explore the salt dynamics in the

559 sub-estuary. In the sub-estuary, the exponential decaying constant of the cross-sectional

560 area was calculated to be 50 km; and the river discharge was specified to be 200 m^3 s$^-$

561 ^{1}.

562 We used the scheme of constant dispersion along the sub-estuary, and the K_x was

563 estimated as (Ralston et al., 2008):

$$K_x = c_h(\frac{T_{tide}}{4}U_T)U_T \tag{9}$$

565 where c_h is an empirical constant of 0.0224, T_{tide} is the tidal period, here is set as

566 12.42 hours; U_T is the tidal current amplitude at the sub-estuary's mouth.

567 We solved Eq. (6) for the model experiment Case 1. The results are shown in Fig.

568 9.
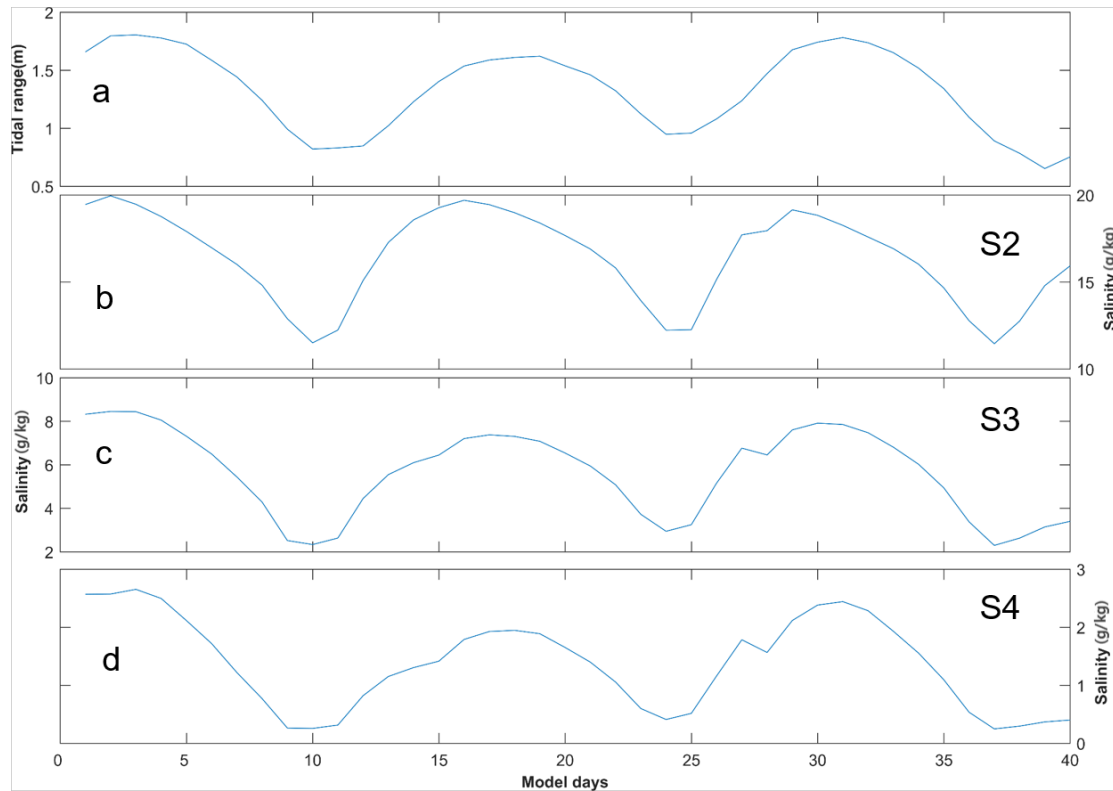
569

Fig. 9. The results of the analytical solution of salinity variations along the sub-estuary. a)

tidal range at the mouth of the sub-estuary; b), c), and d) are tidally-averaged salinity variations

at S2, S3, and S4 stations.

Under the 1500 m^3 s^{-1} river discharge at the head of the main estuary, the tidal

range at the sub-estuary's mouth varies between spring and neap tides, with a greater

spring and a weaker spring in a month (Fig. 9a). The tidally-averaged salinity at the

confluence (S2 station, Fig. 9b) varies between 10 and 20 g/kg, with the maximum

salinities occurring before the spring tides and the minimum salinities before the neap

tides, indicating a phase lead of salinity to the tidal range. In the middle of the sub-

estuary (S3 station, Fig. 9c), the salinity fluctuates between 2 and 10 g/kg, and there

exists a slight phase lead of salinity to that of the tidal range. In the upstream region of

the sub-estuary (S4 station, Fig. 9d), the salinity fluctuates between 0 and 3 g/kg, and

the salinity variation becomes almost in phase with that of the tidal range at the

confluence. Compared to the numerical simulation results, the analytical solution

reproduces the trend of the phase relationship between the salinity and tidal range along

the sub-estuary: the phase of the salinity variation leads that of the tidal range at the

sub-estuary's mouth and becomes more in phase with that of the tidal range in the

middle and upstream region of the sub-estuary. Meanwhile, the fluctuation magnitude

in the middle of the sub-estuary is well reproduced. However, the fluctuation range in

the upstream region of the sub-estuary is over-estimated, showing the weakness of

assuming a uniform horizontal dispersion along the sub-estuary.

5. Discussion

5.1 The physics behind the change in phase relationship between the salinity and tidal range along the sub-estuary

The numerical results and analytical solutions both indicate that near the sub-estuary's mouth, the salinity fluctuation leads that of the tidal range, and in the middle

and upstream region of the sub-estuary, the salinity variation becomes more in phase

with that of the tidal range. The analytical solution shows that the changes in the phase

relationship between these two variables are mostly caused by the change in horizontal

603   dispersion, that is, the larger dispersions during spring tides cause increased landward

604   salt transport, resulting in elevated salinity in the middle and upstream regions of the

605   sub-estuary. The results of numerical simulation are a combination of many

606   interweaved processes and a little harder to interpret. To unravel the physics in the

607   numerical simulation, we examine the salt transport in the lower reach at a cross-section

608   near the sub-estuary mouth and freshwater transport in the upstream cross-section of

609   the sub-estuary (shown in Fig. 2b).
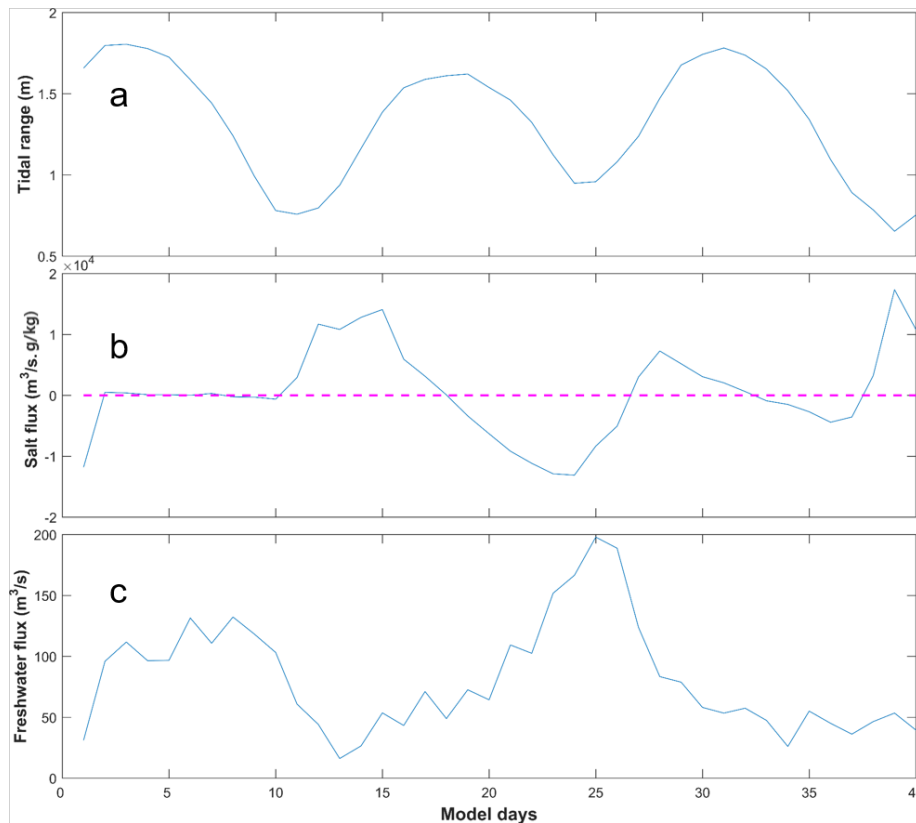
610

611   Fig. 10. Timeseries of: a) tidal range at the mouth of the sub-estuary; b) salt flux at the

612   cross-section near the mouth of the sub-estuary; c) freshwater flux at the cross-section in the

613   upstream region of the sub-estuary. It should be noted that the freshwater flux is the magnitude

614   and has a sign opposite to the salt flux.

615

616   The results are shown in Fig. 10. From Fig. 10b, the tidally-averaged salt flux near

617   the sub-estuary's mouth is generally landward during the periods from neap tides to

618   spring tides and seaward from spring tides to neap tides. The change in salt flux leads

619   that of the tidal range, consistent with the phase relationship between salinity and tidal

620   range near the sub-estuary's mouth (Fig. 8b). As the sub-estuary is well-mixed during

621   the simulation period, the landward salt transport is mostly induced by the tidal

622   oscillatory transport. The tidally-averaged freshwater flux in the upstream region of the

623   sub-estuary is seaward, and shows a pattern that larger freshwater fluxes occur during

624   neap tides and smaller freshwater fluxes during spring tides (Fig. 10c). This pattern has

625   been well studied by Buschman et al. (2009) in the tidally-averaged momentum

626   dynamics. They showed that the primary tidally-averaged momentum balance is

627   between the water level gradient and bottom friction. During spring tides, the tidally-

628   averaged bottom friction is larger and the tidally-averaged water slope is greater,

629   meaning that more freshwater is being detained upstream to elevate the water level

630   there. During neap tides, the detained freshwater in the upstream is released

631   downstream and results in increased freshwater fluxes. In this way, the saline water

632   from the sub-estuary's mouth experiences less impedance and dilution during spring

633   tides and thus advances more landward, resulting in an enhanced salt intrusion during

634   spring tides, and vice versa. The above results indicate that the more in-phase

635   relationship between the salinity and tidal range in the middle and upstream region of

636   the sub-estuary is mostly generated by the fortnightly variation of the tidal strength and

637   the associated variations of horizontal dispersion and freshwater flux by the river-tide

638   interaction. The larger the dispersion, the more salt is pumped into the upstream. The

639   stronger the tidal strength, the more freshwater is detained upstream and less impedance

640   to the salt intrusion.

641   From the above results, it is seen that the salinity dynamics in the sub-estuary show

642   a pattern that is more influenced by the main estuary in the lower reach and becomes

643   more controlled by internal tidal processes in the middle and upstream regions of the

644   sub-estuary.

645

646   5.2 How do the salt dynamics in the main estuary affect that in the sub-estuary?

647

648   To further study how the changes in salinity dynamics in the main estuary affect

649   the salinity variation in the sub-estuary, we set up another experiment. In the model

650   scenario of Case 2, we set an extremely low river discharge (500 m^3 s^{-1}) at the head of

651   the main estuary, and the results are shown in Fig. 11. Simultaneously, the analytical

652   solutions for the scenario of Case 2 are presented in Fig. 12.
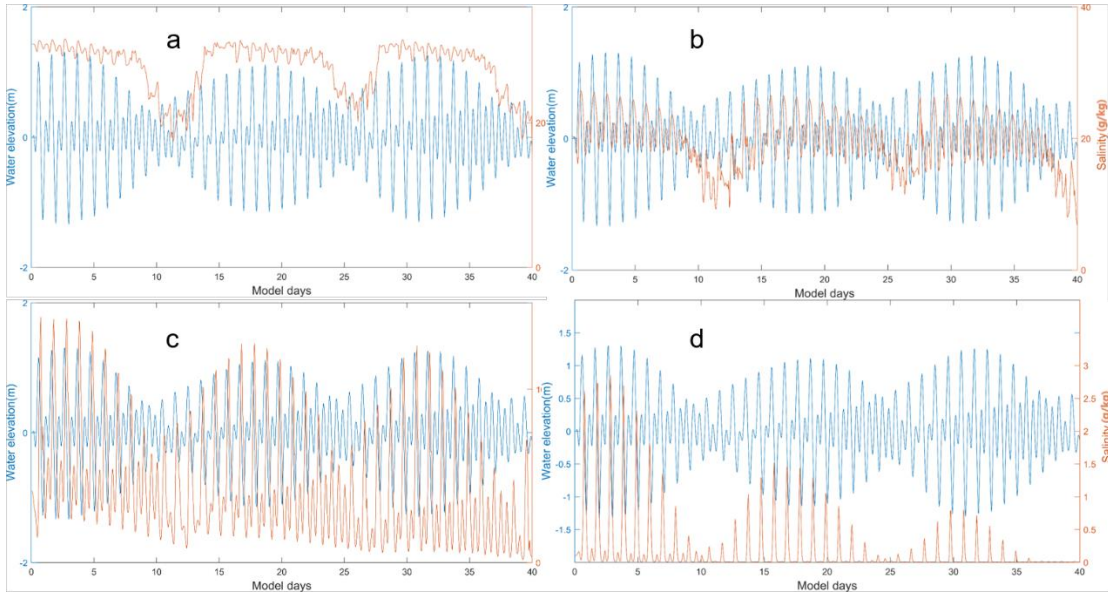
Fig. 11. Timeseries of water level at the confluence and surface salinity under the

extremely low river discharge in the main estuary at stations of: a) S1; b) S2; c) S3; d) S4.
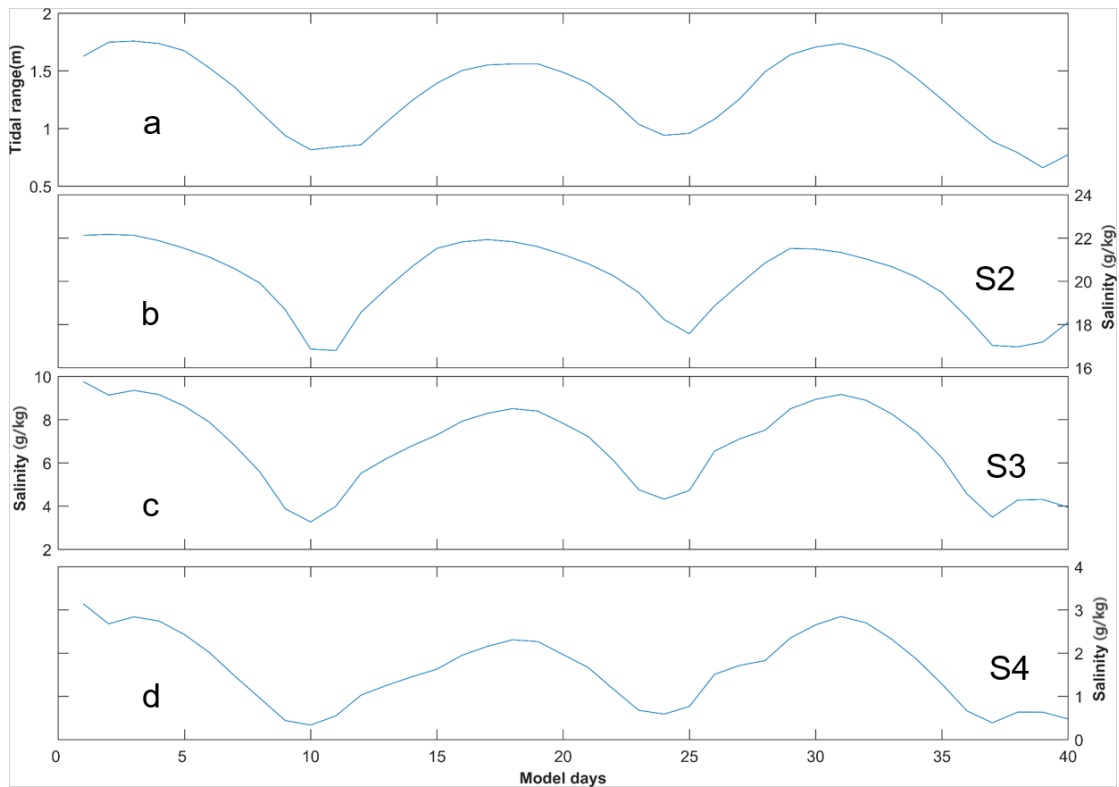
Fig. 12. The results of the analytical solution of salinity variations along the sub-estuary under extremely dry conditions. a) tidal range at the mouth of the sub-estuary; b), c), and d) are tidally-averaged salinity variations at S2, S3, and S4 stations.

With decreased river discharge from the head of the main estuary, the salt intrusion front is shifted more landward. The S1 station is now located in the polyhaline region with a mean salinity of approximately 26 g/kg (Fig. 11a). The minimum salinities coincide more with neap tides but the maximum salinities occur around spring tides. The asymmetry between salinity rise and fall is decreased, with salinities jumping quickly after neap tides, keeping elevated around spring tides, and dropping quickly just before neap tides. For the intratidal variation, it can be seen that during a tidal cycle, the salinity fluctuation is reduced when compared to Case 1 (Figs. 11a vs 8a), which is mostly due to the fact that with the reduced river discharge, the salinity gradient in the polyhaline reach of the main estuary is decreased.

For the S2 Station (at the confluence, Figs. 11b and 12b), it is now located in the mesohaline region, with the salinity ranging from 5 to 26 g/kg. The highest and lowest salinities are both increased when compared to Case 1, with a reduced magnitude of salinity change in a tidal cycle. The salinity variation pattern remains similar to that in Case 1, with minimum salinities occurring just before neap tides, and maximum salinities after neap tides, but occur closer to spring tides. The asymmetry of quick

678 increase from neap to spring but gradual decrease afterwards is still clear.

679 When entering into the sub-estuary, the salinity variation at S3 in the middle of the

680 sub-estuary shows a more in-phase relationship between salinity and tidal range (Figs.

681 11c and 12c). The maximum salinities occur closer to spring tides whereas the

682 minimum salinities still occur just before neap tides. In the upstream region of the sub-

683 estuary (Figs. 11d and 12d), the phase relationship between salinity and tidal range is

684 also an in-phase one. Combined with the situation at the S1 Station, it indicates that the

685 variations of salinity at stations S4 and S1 are more synchronous. This largely explains

686 the observed phenomenon that under more drought conditions, the salinity variations at

687 the Second Water Plant kept pace with those at the Dahu Station (Section 3.1).

688

689 **5.3 Limitations and implications of this study**

690

691 In this study, we focus on the phase relationship between the variations of salinity

692 and tidal range, both in a sub-estuary and the main estuary. The salinity variations along

693 the sub-estuary are revealed to be associated with the salinity dynamics in the main

694 estuary, linked by the salinity variations at the confluence between the main estuary and

695 the sub-estuary. In a spring-neap tidal cycle, even when the salinity at the confluence is

696 a little lower during the spring tide than that during the neap tide, the higher horizontal

697 dispersion and decreased freshwater release at the head of the sub-estuary during the

698 spring tide can pump more saline water from the confluence into the middle and

699   upstream of the sub-estuary, and cause the salinities there to be higher than during the

700   neap tide. In this way, the salinity variations at areas farther away from the confluence

701   become more synchronous with the tidal range.

702   However, this study did not consider the effect of winds and waves, as shown to

703   be important in previous studies such as Gong et al. (2018). The variations of salinity

704   in the period of 5-8 days should be related to the wind effects and await future

705   exploration. The effect of sea level change outside the main estuary was also not

706   examined in detail, though it can be intrinsically linked to the effect of winds and waves.

707   Finally, we did not explore a full parameter space of river discharge, tidal range, and

708   bathymetry situations, and thus can not give a synthesis of the sub-estuary salt intrusion

709   dynamics at this time.

710   Despite all these limitations, this study has implications for studying salt intrusion

711   dynamics in sub-estuaries, which are influenced by both the hydrodynamics inside the

712   sub-estuary and the salt dynamics in the main estuaries. It is also of importance for

713   providing a scientific basis for salt intrusion mitigation in the region. For example, salt

714   intrusion in the sub-estuary is not only impacted by the river discharge from the head

715   of the sub-estuary itself but also largely affected by the salt dynamics in the main estuary.

716   In this respect, apart from releasing more freshwater from the upstream in the sub-

717   estuary, measures to control the salinity variations at the confluence between the main

718   estuary and the sub-estuary also need to be taken into consideration. This may involve

719   implementing engineering solutions such as the construction of barriers or gates to

720   regulate the inflow of saltwater from the main estuary into the sub-estuary. Additionally,

721   the management of water withdrawals and releases in the sub-estuary and main estuary

722   needs to be optimized by taking the estuarine system as a whole. Overall, a

723   comprehensive and coordinated approach is necessary to effectively mitigate salt

724   intrusion in sub-estuaries.

725

726   **6. Summary and conclusions**

727

728   From 2021 to 2022, under the influence of an extended La Nina event, the Pearl

729   River Delta region in China experienced a prolonged extreme drought condition, and

730   the sub-estuary (East River estuary) also suffered greatly from the enhanced salt

731   intrusion. To identify the characteristics of the salt intrusion in the sub-estuary, and to

732   explore the underlying physics in controlling the spatio-temporal variations of the salt

733   intrusion, we collected observation data and conducted numerical simulations for

734   idealized estuarine bathymetry, and used analytical solutions for the tidally-averaged

735   salinity variations in the sub-estuary. The observation data showed that the salinity

736   variation in the main estuary usually led that of the tidal range, and the asymmetry

737   between salinity rise and fall in a fortnightly timescale was prominent. However, in the

738   upstream region of the sub-estuary, the salinity variation was in phase with that of the

739   tidal range, and the salinity rise and fall were more symmetrical. The idealized model

740   simulations and the analytical solution both reproduced these phenomena.

741   We note that under drought conditions, the river-tide interaction played a role in

742 the in-phase relationship between the salinity and tidal range in the upstream region of

743 the sub-estuary. The salinity variation in the middle and upstream regions of the sub-

744 estuary can keep pace with that of the tidal range. The analytical results show that the

745 horizontal dispersion scaling with tidal strength can largely reproduce the changes in

746 phase relationship between salinity and tidal range in the sub-estuary. We conclude that

747 both the changes in horizontal dispersion and the river-tide interaction in modulating

748 the freshwater release are responsible for the in-phase relationship between the salinity

749 and tidal range in the middle and upstream regions of the sub-estuary.

750   This study is of help in the investigation of salt dynamics in sub-estuaries

751 connected to main estuaries, and of implications for mitigating salt intrusion problems

752 in the regions suffered from enhanced salt intrusion by climate change and human

753 interventions.

754

755 **Data availability:** The observation data can be downloaded from the website

756 http://www.pearlwater.gov.cn/. The numerical data is available upon request to the

757 corresponding author.

758

759 **Declaration of competing interest**

760   The contact author has declared that none of the authors has any competing

761 interests.

762

763   **CRediT authorship contribution statement**

764   **Zhongyuan Lin:** Data collection, wavelet analysis, Writing - original draft,

765 Writing - review & editing. **Guang Zhang:** numerical modeling, Writing - review &

766 editing. **Huazhi Zou**: Writing-review &editing, funding acquisition. **Wenping Gong**:

767 Conceptualization, Methodology, Writing-review &editing, funding acquisition.

768

769 **Acknowledgments**

770

771   This research was funded by the National Natural Science Foundation of China

772 (grant numbers 42276169, 42306015) and The Science and Technology Innovation

773 Program from Water Resources of Guangdong Province (2023-01). Savenije, H.H.G.

774 at the Delft University of Technology and another anonymous reviewer are greatly

775 appreciated for their constructive comments and suggestions to improve this manuscript.

776 We would also like to thank the editor Huthnance, J. for his great insights in the

777 scientific issues raised in this manuscript.

778

779 **Supplement:**

780

781   We present the longitudinal profiles of tidally-averaged current and salinity along the

782 channels in the main estuary and the sub-estuary during typical spring and neap tides.

783 Fig. S1 is for the dry condition with 1500 m^3/s at the head of the main estuary, and Fig.

784 S2 for the extremely dry condition with 500 m^3/s released at the head of the main estuary.

785

786 **References**

787 Bowden, K. F.: Horizontal mixing in the sea due to a shearing current, J. FLUID.

788   MECH., 21, 83-95, https://doi.org/10.1007/BF00167972, 1965.

789 Bowen, M., and Geyer, W.R.: Salt transport and the time-dependent salt balance of a

790   partially stratified estuary, J. GEOPHYS. RES., 108(C5),

791   3185,https://doi:10.1029/2001JC001231, 2003.

792 Buschman, F. A., Hoitink, A. J. F., and Vegt., M. V. D.: Subtidal water level variation

793   controlled by river flow and tides, WATER. RESOUR. RES., 45(10),

794   W10420,https://doi.org/10.1029/2009WR008167, 2009.

795 Cai, H., Savenije, H.H.G., Zuo, S., Jiang, C., and Chua, V.P.: A predictive model for

796   salt intrusion in estuaries applied to the Yangtze estuary, J. HYDROL., 529,

797   1336-1349, https://doi.org/10.1016/j.jhydrol.2015.08.050, 2015.

798 Chapman, D. C.: Numerical Treatment of Cross-Shelf Open Boundaries in a Barotropic

799   Coastal Ocean Model, J. PHYS. OCEANOGR., 15(8), 1060-1075,

800   https://doi.org/10.1175/1520-0485(1985)015<1060:NTOCSO>2.0.CO;2, 1985.

801 Chen S.-N.: Asymmetric Estuarine Responses to Changes in River Forcing: A

802   Consequence of Nonlinear Salt Flux, J. PHYS. OCEANOGR., 45(11), 2836-2847,

803   https://doi.org/10.1175/JPO-D-15-0085.1., 2015.

804 Dong, L., Su, J., Wong, L., Cao, Z., and Chen, J.-C.: Seasonal variation and dynamics

of the Pearl River plume, CONT. SHELF. RES., 24(16), 1761-1777, https://doi.org/10.1016/j.csr.2004.06.006, 2004.

Du, J., Park, K.: Estuarine salinity recovery from an extreme precipitation event: Hurricane Harvey in Galveston Bay, SCI. TOTAL. ENVIRON., 670, 1049-1059, https://doi.org/10.1016/j.scitotenv.2019.03.265, 2019.

Flather, R. A.: A tidal model of the northwest European continental shelf, Mem. Soc. R. Sci. Liege,, 10(6), 141-164, 1976.

Gong, W., and Shen, J.: The response of salt intrusion to changes in river discharge and tidal mixing during the dry season in the Modaomen Estuary, China, CONT. SHELF. RES., 31, 769–788, https://doi.org/10.1016/j.csr.2011.01.011, 2011.

Gong, W., Lin, Z., Chen, Y., Chen, Z., and Zhang, H.: Effect of winds and waves on salt intrusion in the Pearl River estuary, OCEAN. SCI., 14(1), 139-159, https://doi.org/10.5194/os-14-139-2018, 2018.

Gong, W., Chen, L., Zhang, H., Yuan, L., and Chen, Z.: Plume Dynamics of a Lateral River Tributary Influenced by River Discharge From the Estuary Head, J. GEOPHYS. RES-OCEANS., https://doi.org/10.1029/2019JC015580, 2020.

Gong, W., Lin, Z., Zhang, and H., Lin H.: The response of salt intrusion to changes in river discharge, tidal range, and winds, based on wavelet analysis in the Modaomen estuary, China, OCEAN. COAST. MANAGE., 219, 106060, https://doi.org/10.1016/j.ocecoaman.2022.106060, 2022.

825 Haidvogel, D. B., Arango, H. G., Hedstrom, K., Beckmann, A,.Malanotte-Rizzoli, B.,

826   Shchepetkin, and A., F.: Model evaluation experiments in the North Atlantic Basin:

827   Simulations in nonlinear terrain-following coordinates, DYNAM.   ATMOS.

828   OCEANS., 32(3-4), 239-281, https://doi.org/10.1016/S0377-0265 (00)00049-X,

829   2000.

830 Haywood, D., Welch, C. S., and Hass, L. W.: York River destratification: an estuary-

831   sub-estuary   interaction,   Science,   216,   1413-1414,

832   https://doi.org/10.1126/science.216.4553.1413, 1982.

833 Hong, B., Liu, Z., Shen, J., Wu, H., Gong, W., Xu, H., and Wang, D.: Potential physical

834   impacts of sea-level rise on the Pearl River Estuary, China, J. MARINE. SYST.,

835   201, 103245, https://doi.org/10.1016/j.jmarsys.2019.103245, 2020.

836 Hu, J., Li, S., and Geng, B.: Modeling the mass flux budgets of water and suspended

837   sediments for the river network and estuary in the Pearl River Delta, China,   J.

838   MARINE. SYST., 88(2), 252-266, https://doi.org/10.1016/j.jmarsys.2011.05.002,

839   2011.

840 Jia, L., Luo, Z., Yang, Q., Ou, S., and Lei, Y.: The impact of massive sand mining on

841   the morphology and tidal dynamics in the downstream of East River and the East

842   River Delta (In Chinese), Acta Geographica Sinica, 09, 985-994, 2006.

843 Liu, B., Yan, S., Chen, X., Lian, Y., and Xin, Y.: Wavelet analysis of the dynamic

844   characteristics of saltwater intrusion - A case study in the Pearl River Estuary of

China, OCEAN. COAST. MANAGE., 95, 81-92, https://doi.org/10.1016/j.ocecoaman.2014.03.027, 2014.

MacCready, P., and Geyer, W. R.: Advances in estuarine physics, ANNU. REV. MAR. SCI., 2(1), 35–58, https://doi.org/10.1146/annurev-marine-120308-081015, 2010.

Mao, Q., Shi, P., Yin, K., Gan, J., and Qi, Y.: Tides and tidal currents in the Pearl River Estuary, CONT. SHELF. RES., 24(16), 1797-1808, https://doi.org/10.1016/j.csr.2004.06.008, 2004.

Okubo, A.: Effect of shoreline irregularities on streamwise dispersion in estuaries and other embayments, NETH. J. SEA. RES., 6, 213-224, https://doi.org/10.1016/0077-7579 (73)90014-8, 1973.

Orlanski, I.: A simple boundary condition for unbounded hyperbolic flows. J. COMPUT. PHYS., 21(3), 251–269, http://dx.doi.org/10.1016/0021-9991(76)90023-1, 1976.

Payo-Payo, M., Bricheno, L. M., Dijkstra, Y. M., Cheng, W., Gong, W., and Amoudry, L. O.: Multiscale temporal response of salt intrusion to transient river and ocean forcing, J. GEOPHYS. RES-OCEANS., 127, e2021JC017523, https://doi. org/10.1029/2021JC017523, 2022.

Ralston, D. K., Geyer, and W. R., Lerczak J. A.: Structure, variability, and salt flux in a strongly forced salt wedge estuary, J. Geophys. Res., 115, C06005,

865 doi:10.1029/2009JC005806, 2010.

866 Ralston, D. K., and Geyer, W. R.: Response to channel deepening of the salinity

867 intrusion, estuarine circulation, and stratification in an urbanized estuary, J.

868 GEOPHYS. RES-OCEANS., 124, 4784–4802,

869 https://doi.org/10.1029/2019JC015006, 2019.

870 Savenije, H.H.G., 2012. Salinity and tides in alluvial estuaries. Second Edition

871 <www.salinityandtides.com>.

872 Shchepetkin, A. F., and McWilliams, J. C.: The regional ocean modeling system

873 (ROMS): A split-explicit, free-surface, topography-following coordinates oceanic

874 model, OCEAN. MODEL., 9, 347–404,

875 https://doi.org/10.1016/j.ocemod.2004.08.002, 2005.

876 Simpson, J.H., Brown, J., Matthews, J.P., and Allen, G.: Tidal straining, density currents,

877 and stirring in the control of estuarine stratification, ESTUARIES, 13 (2), 125–

878 132, 1990.

879 Smagorinsky, J.: General Circulation Experiments with the Primitive Equation, Part 1,

880 the Basic Experiment, MON. WEATHER. REV., 91(3), 99-164,

881 http://dx.doi.org/10.1175/1520-0493, 1963.

882 Spinoni, J., Naumann, G., Carrao, H., Barbosa, P., and Vogt, J.: World drought

883 frequency, duration, and severity for 1951–2010, INT. J. CLIMATOL., 34(8),

884 2792–2804, https://doi.org/10.1002/joc.3875, 2014.

Stommel, H., and Farmer, H. G. On the nature of estuarine circulation: part I (chapters 3 and 4), Woods Hole Oceanographic Institution, 1952.

Umlauf, L., and Burchard, H.: A generic length-scale equation for geophysical turbulence models, J. MAR. RES., 61(2), 235-365, https://doi.org/10.1357/002224003322005087, 2003.

Uncles, R. J., and Stephens, J. A.: Turbidity and sediment transport in a muddy sub-estuary, ESTUAR. COAST. SHELF. S., 87(2), 213-224, https://doi.org/10.1016/j.ecss.2009.03.041, 2010.

Warner, J. C., Sherwood, C. R., Arango, H. G., and Signell, R. P., Butman, B. Performance of four turbulence closure models implemented using a generic length scale method, OCEAN. MODEL., 8, 81–113, 2005.

Wei, X., Kumar, M., and Schuttelaars, H.M.: Three-dimensional salt dynamics in well-mixed estuaries: influence of estuarine convergence, Coriolis, and bathymetry, J. PHYS. OCEANOGR., 47, 1843-1872, https://doi.org/10.1016/j.ocemod.2003.12.003, 2017.

Wong, L. A., Chen, J. C., Xue, H., Dong, L. X., Su, J. L., and Heinke, G.: A model study of the circulation in the Pearl River Estuary (PRE) and its adjacent coastal waters: 1. Simulations and comparison with observations, J. GEOPHYS. RES., 108(C5), https://doi.org/10.1029/2002jc001451, 2003.

Wu, Z. Y., Saito, Y., Zhao, D. N., Zhou, J. Q., Cao, Z. Y., and Li, S. J.: Impact of human

activities on subaqueous topographic change in Lingding Bay of the Pearl River estuary, China, during 1955-2013, SCI. REP-UK., 6, 37742, https://doi.org/10.1038/srep37742, 2016.

Yellen, B., Woodruff, J. D., Ralston, D. K., MacDonald, and D. G., Jones. D. S.: Salt wedge dynamics lead to enhanced sediment trapping within side embayments in high-energy estuaries, J. GEOPHYS. RES-OCEANS., 122(3), 2226-2242, https://doi.org/10.1002/2016JC012595, 2017.

Zhang, P., Yang, Q., Wang, H., Cai, H., Liu, F., Zhao, T., and Jia, L.: Stepwise alterations in tidal hydrodynamics in a highly human-modified estuary: The roles of channel deepening and narrowing, J. HYDROL., 597, 126153, https://doi.org/10.1016/j.jhydrol.2021.126153, 2021.

Zimmerman, J. T. F.: The tidal whirlpool: A review of horizontal dispersion by tidal and residual currents, NETH. J. SEA. RES., 20, 133-154, https://doi.org/10.1016/0077-7579(86)90037-2, 1986.

Figure Captions:

Fig.1. a) The East River estuary; b) Map of the Pearl River Delta and the locations of hydrological and water level stations.

Fig. 2. Geometry and bathymetry of the idealized model domain: a)for the whole domain; b)zoom in for the area of concern. The origin of the coordinates is in the middle of the main estuary mouth. The longitudinal sections in the main and sub-estuary are shown as dashed lines, and the cross-sections inside the sub-estuary are shown as color solid lines. The locations of several stations are indicated.

Fig.3. Timeseries of: a) Daily maximum salinity at the Second Water Plant; b) Total duration period with salinity exceeding 0.5 g/kg for each month; c) Monthly river discharge at Boluo station (upstream of the East River); d) Monthly river discharge at Wuzhou station (upstream of the West River); e) Monthly river discharge at Shijiao station (upstream of the North River).

Fig. 4 Wavelet analysis of the salinity at the Second Water Plant.

Fig. 5. Timeseries of: a) Daily maximum salinity at the Second Water Plant; b) Daily river discharge at Boluo station; c) Daily maximum tidal range at Sishengwei Station; d) Daily maximum salinity at Dahu Station; e) Daily mean sea level at Shibi Station.

Fig. 6. Cross-wavelet analysis of (a) between the salinity at Dahu and the tidal

range at Sishengwei; (b) between the salinity at the Second Water Plant and the tidal range at Sishengwei; (c) between the salinity at the Second Water plant and the river discharge at the Boluo Station; (d) between the salinity at the Second Water plant and that at the Dahu Station.

Fig. 7. Timeseries of: a) tidal range at the mouth of the main estuary; b) salt intrusion length along the longitudinal section of the main estuary; c) salt intrusion length along the longitudinal section of the sub-estuary.

Fig. 8. Timeseries of water level at the confluence and surface salinity a) at S1 Station in the main estuary; b) at S2 station (the confluence); c) at S3 station in the middle of the sub-estuary; d) at S4 station in the upstream region of the sub-estuary.

Fig. 9. The results of the analytical solution of salinity variations along the sub-estuary. a) tidal range at the mouth of the sub-estuary; b), c), and d) are tidally-averaged salinity variations at S2, S3, and S4 stations.

Fig. 10. Timeseries of: a) tidal range at the mouth of the sub-estuary; b) salt flux at the cross-section near the mouth of the sub-estuary; c) freshwater flux at the cross-section in the upstream region of the sub-estuary.

Fig. 11. Timeseries of water level at the confluence and surface salinity under the extremely low river discharge in the main estuary at stations of: a) S1; b) S2; c) S3; d) S4.

Fig. 12. The results of the analytical solution of salinity variations along the sub-

962   estuary under extremely dry conditions. a) tidal range at the mouth of the sub-estuary;

963   b), c), and d) are tidally-averaged salinity variations at S2, S3, and S4 stations.

964